Paul M. Nadan
Olin College of Engineering,
1000 Olin Way,
Needham, MA 02492

Tatiana M. Anthony
Olin College of Engineering,
1000 Olin Way,
Needham, MA 02492

Duncan M. Michael
Olin College of Engineering,
1000 Olin Way,
Needham, MA 02492

Jeffrey B. Pflueger
Olin College of Engineering,
1000 Olin Way,
Needham, MA 02492

Manik S. Sethi
Olin College of Engineering,
1000 Olin Way,
Needham, MA 02492

Kelli N. Shimazu
Olin College of Engineering,
1000 Olin Way,
Needham, MA 02492

Mindy Tieu
Olin College of Engineering,
1000 Olin Way,
Needham, MA 02492

Christopher L. Lee[2]
Mem. ASME
Olin College of Engineering,
1000 Olin Way,
Needham, MA 02492
e-mail: christopher.lee@olin.edu

A Bird-Inspired Perching Landing Gear System[1]

The design, modeling, simulation, and testing of a landing gear system that enables a UAV to perch on an object or surface is presented here. The working principle of the landing gear is inspired by the anatomy of birds that grasp and perch as tendons in their legs and feet are tensioned. In a similar fashion, as the UAV sets down on a structure, its weight tensions a cable which actuates opposing, flexible, multi-segment feet to enclose the target. To analyze the grasping capability of the design, a hybrid empirical–computational model is developed that can be used to simulate the kinematics of the system as it grasps objects of various cross-sectional shapes and sizes. The model relates the curvature of the feet to the displacement and tension of the cable tendon. These quantities are then related to the weight of the UAV through the leg geometry. It also evaluates enclosure and calculates contact forces to quantitatively characterize the grasp. Results demonstrate how the model can be used by designers to determine how a UAV can perch upon a structure of a given shape and size. If perched, the minimum weight required to maintain its position is calculated. A prototype system was fabricated, analyzed, and tested on a radio-controlled hexacopter. Experiments show that the landing gear enables the hexacopter to land, perch, and takeoff from a variety of objects. Finally, we begin to investigate the scalability of the concept with a smaller, lighter design. [DOI: 10.1115/1.4044416]

Keywords: bioinspired design, cable-driven mechanisms, grasping and fixturing

1 Introduction

Small unmanned aerial vehicles (UAV) are used in a wide and rapidly growing range of civil and military applications. Missions often call for operation in urban or rural settings that do not have appropriate or sufficiently large space for takeoff and landing. In such areas, the capability for a UAV to land, perch, and take off from available structures and surfaces would enable it to perform its missions.

To smoothly alight on a structure like a bird, a UAV has to execute a series of intricate flight maneuvers involving complex path planning and trajectory control [3]. To study this, Robertson and Reich [4] conducted controlled flight tests to land and perch small fixed-wing planes with bird-like planforms on a target platform. Nagendran et al. [5] evaluated controllers for softly landing a UAV with a two-joint leg on a surface. Paranjape et al. [6] designed and experimentally demonstrated a guidance and control scheme to land and perch a fixed-wing micro aerial vehicle equipped with articulated wings. In Ref. [7], Cory and Tendrake designed and tested optimal control policies for the elevator deflection of a small fixed-wing autonomous glider so it could execute high angle-of-attack maneuvers needed to land on a suspended horizontal string.

In addition to controlling their flight to perch, birds use their feet to grasp ahold of the structures or objects that they are landing on. UAV's can do likewise by employing a clamping or grasping mechanism. Culler et al. [8] designed and tested a compliant, bistable snapping-claw mechanism that is triggered by the impact of landing. In Ref. [9], Ali Erbil et al. used a design optimization procedure to identify a configuration for a four-legged, motor-driven gripper that can clamp onto a cylindrical projection bracket. Using a two-dimensional model to guide their designs, Chi et al. [10] developed and tested a mechanically similar, four-legged,

---

servo-driven gripper. Jiang et al. [11] created a model of an opposing-grip mechanism with adhesive contact surfaces embedded with micro-spines for perching on walls and ceilings. They conducted experiments to validate mechanical aspects of their model. Burroughs et al. [12] modeled, fabricated, and tested a Sarrus-linkage-based clamping mechanism for a rotorcraft to perch on various objects. The mechanism is actuated by the weight of the air vehicle.

This passive actuation is the working principle for the legs of many types of birds [13]. When landing and coming to a rest, the joints in the bird's legs rotate and the bird's weight tensions tendons causing the foot to enclose the object it wraps around. When the bird takes off, the tendons relax from their stretched position and the grasp is released. Backus et al. [14] modeled the grasping behavior of a robot hand to analyze the forces imparted when carrying a payload or perching on a fixed object in order to evaluate its performance. In Ref. [15], they performed mechanical analysis on a tendon-actuated avian foot to determine the effects that geometric parameters have on grasping and perching. Doyle et al. [16] presented work on a perching mechanism based upon a collapsing leg with tendon-actuated gripping feet. They developed a model that relates tendon pull to foot joint deflections when gripping an object with a circular cross section. Static tests demonstrated that a quadcopter could successfully perch on a variety of commonly available objects. Xie and Ma [17] and Xie et al. [18] presented the design of a collapsible-leg mechanism with cable-tensioned feet. A geometric model was used to show how the digits of the feet would come in contact with a cylindrical cross section. A prototype of a foot could grasp a wide variety of objects; however, the force applied was significantly reduced by friction in the joints. In addition, the entire leg–foot system was too large and heavy to incorporate in a small UAV.

This paper presents the design, modeling, analysis, and testing of a landing gear system that enables a small UAV to grasp and perch upon branches or similar structures. This system uses opposing, cable-tendon-actuated, multi-segmented feet to grasp a given landing target. To support the design process, a hybrid empirical–numerical model for a fabricated prototype is developed that can simulate the system grasping objects with a range of cross-sectional shapes, dimensions, and orientations. The resulting kinematics and kinetics (e.g., contact forces) are evaluated by quantifying the completeness of the enclosure of the target object and the strength of the grasp. Experimental results are presented that demonstrate that the prototype system attached to a radio-controlled hexacopter can stably perch on a range of structures and can land on or take off from a perch. The primary novelty herein is the extension of the initial model development [1] and prototype testing [2] to the validation, analysis, and evaluation of grasping simulations for a variety of landing targets.

2 Perching Landing Gear System Design and Prototype

A bird-inspired landing gear system attached to the frame of a hexacopter (details are given in Sec. 5) is shown in Fig. 1. Each of the two legs of the landing gear is a four-bar linkage that is connected to the airframe by a revolute joint in the hips. At the bottom of each leg are two opposing, flexible feet with rigid heels. The feet are offset relative to one another; see Fig. 2.

The feet (an example is shown in Fig. 3) are single, compliant structures fabricated by simultaneously 3D-printing a flexible thermoplastic (NinjaFlex, Fenner Drives, Manheim, PA) and a stiff plastic (ABS, Makerbot, Brooklyn, NY). Six stiff trapezoidal segments (i.e., phalanges) are connected together to a base segment by two flexible rails. Both feet are actuated by a single cable (Trilene XT 30 lbs., Berkeley Fishing, Spirt Lake, IA) tendon. As shown in the routing diagram, Fig. 4, one end of a length of cable is tied off on the underside of the claw segment of one foot. It passes through each segment of the foot, wraps around pulleys at joints of the four-bar linkage, and then passes through the other foot segments where it is tied off at the other claw segment. As the UAV lands, the four-bar linkage collapses pulling the cable
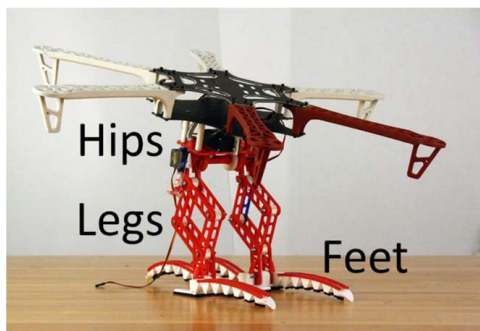

Fig. 1 Prototype of a bird-inspired, perching landing gear system consisting of four-bar-linkage legs with multi-segmented, flexible feet. The legs are connected to the frame of a hexacopter by a revolute joint in the hips.

Fig. 3 A seven-segment, compliant foot fabricated by 3D-printing a flexible thermal-plastic and a stiff plastic. Length = 13 cm, range of segment heights = 0.9–1.7 cm, and mass = 9.7 g.

Fig. 2 The hexacopter frame perched on a wood beam. Each leg has two opposing, offset, flexible feet with rigid heels.
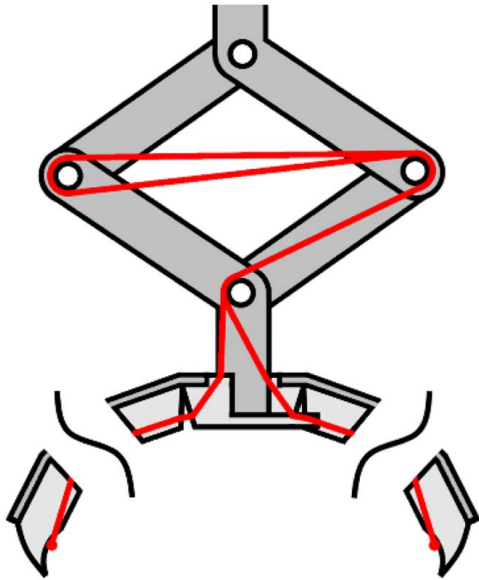
Fig. 4 Cable tendon routing diagram. A single cable wraps around joints in the legs, passes through each foot segment, and is tied off on the claw segments at the ends of both feet.

tendon which causes the feet to curl and grasp the landing target. Two design features prevent the claw end from curling closed before the target can be grasped. First, the height of each segment is graduated from highest near the base to lowest at the claw end creating larger bending moments on the rails toward the base.
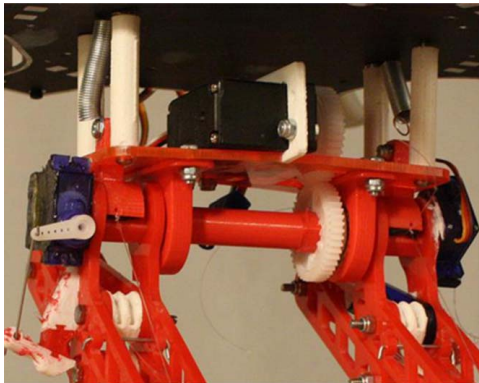

Fig. 5 A servomotor between the hips of the landing gear and aircraft frame can rotate the legs. When the aircraft comes to rest, a clamp engages, which prevents the legs from rotating.

Fig. 6 The hexacopter frame with the legs of the landing gear at different angles is lowered onto a wood beam

Second, the rails themselves taper slightly going from the claw end back to the base. The area moment of inertia of the cross section decreases which decreases the bending stiffness toward the base. Soft pads were attached to the faces of each segment to improve their grip during testing.

A servo motor (see Fig. 5) can rotate the axle of the revolute joint in the hips through a pair of gears so that the legs can be positioned over a range of approach angles. In Fig. 6, the prototype, suspended from strings like a marionette, is lowered down with the legs at different angles to grasp a wood beam. When the aircraft comes to rest, a clamp engages with the axle to prevent it from rotating and holds the legs in place.

Two small servomotors are mounted on the outside of each leg, as shown in Fig. 7. These servos engage/disengage a latch, 3D-printed with ABS and NinjaFlex for flexibility, which locks the legs in the collapsed position. The lock fixes the grasp and prevents release if the aircraft is subject to an upward or overturning disturbance. The mass of one set of legs and feet is 89.2 g where the four-bar linkage is 53.9 g, one foot is 9.7 g, and the servo motor is 11 g.

3 Empirical–Numerical Model of Grasping

To support the design process, a hybrid empirical–numerical model has been created that can be used to simulate and evaluate the mechanical behavior of a planar abstraction of the landing gear system. To demonstrate, a model is generated for the prototype mechanism shown in Fig. 1. A flowchart listing each step of the process to simulate and evaluate the kinematics of the grasping action and then kinetically evaluate the success and strength of the resulting grasp is shown in Fig. 8. The model requires empirical relationships (e.g., cubic polynomials) to be found that relate the relative rotation angles of the segments of the feet to the tendon displacement and relate the tendon displacement to the tendon tension. Mathematical details for each step are presented in Secs. 3.1–3.5.

3.1 Four-Bar Linkage Equations. As the four-bar linkage (see Fig. 9) collapses under the weight of the UAV, the distance between joints J_1 and J_3 increases, causing a reduction in the length of the tendon within the foot. The collapse kinematics are simulated in MATLAB (MathWorks, Natick, MA) using the following vector loop equations

$$L_1 \sin(\theta_1) + L_2 \sin(\theta_2) + L_3 \sin(\theta_3) + L_4 \sin(\theta_4) = 0$$
$$L_1 \cos(\theta_1) + L_2 \cos(\theta_2) + L_3 \cos(\theta_3) + L_4 \cos(\theta_4) = 0 \qquad (1)$$

The sum of the position vectors of each link equals zero because they form a closed loop. Taking the derivative of Eq. (1) with respect to time while holding θ_1 constant yields

$$L_2 \cos(\theta_2)\omega_2 + L_3 \cos(\theta_3)\omega_3 + L_4 \cos(\theta_4)\omega_4 = 0$$
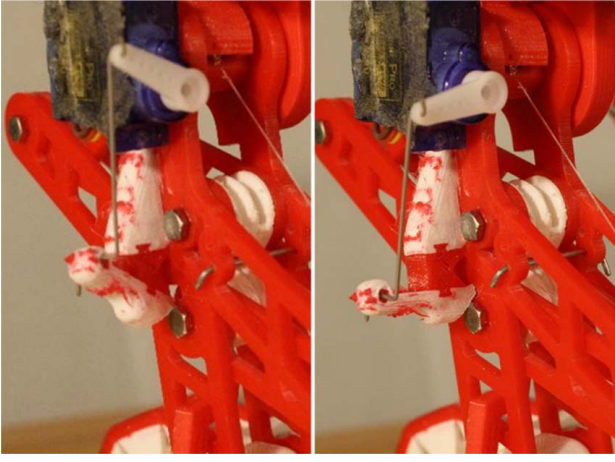$$-L_2 \sin(\theta_2)\omega_2 - L_3 \sin(\theta_3)\omega_3 - L_4 \sin(\theta_4)\omega_4 = 0 \qquad (2)$$

Fig. 7 The legs of the landing gear can be locked into position by a latch that is engaged (right) or disengaged (left) with a servomotor

Fig. 9 Diagram of the four-bar linkage. For the prototype, $L_1 = L_3 = 5.71$ cm and $L_2 = L_4 = 6.35$ cm.

and J_3, to be calculated as

$$x = |J_1 - J_3| - l_0 \qquad (5)$$

where l_0 is the distance between joints J_1 and J_3 in the linkage's initial configuration.

3.2 Tendon Tension and Segment Angle Relationship. The tension in the cable tendon and the relative angles, ϕ_i between each segment of the foot (shown in Fig. 10) are related through the displacement of the tendon. The tension in the tendon was measured with a force gage as it was displaced by a known amount; see Fig 11. Similarly, the (relative) segment angles were determined

where ω_i is the angular velocity of each link. The angular velocities ω_3 and ω_4 can be written in terms of ω_2 and the current linkage angles by recasting Eq. (2) as

$$\begin{bmatrix} \omega_3 \\ \omega_4 \end{bmatrix} = \begin{bmatrix} L_3 \sin(\theta_3) & L_4 \sin(\theta_4) \\ L_3 \cos(\theta_3) & L_4 \cos(\theta_4) \end{bmatrix}^{-1} \begin{bmatrix} -L_2 \sin(\theta_2)\omega_2 \\ -L_2 \cos(\theta_2)\omega_2 \end{bmatrix} \qquad (3)$$

Taking ω_3 to be constant, the linkage geometry can be calculated numerically [19] over the duration of the collapse starting from a known initial configuration.

The simulation is terminated when the angle θ_2 reaches the maximum value allowed by the geometry of the mechanism. The position of each joint can be computed for any state of the linkage using the resulting position vectors

$$J_n = \sum_{i=1}^{n} L_i \cos(\theta_i)\hat{i} + L_i \sin(\theta_i)\hat{j} \qquad (4)$$

The tendon is taken to be inextensible, allowing the tendon displacement, x defined as the change in distance between joints J_1
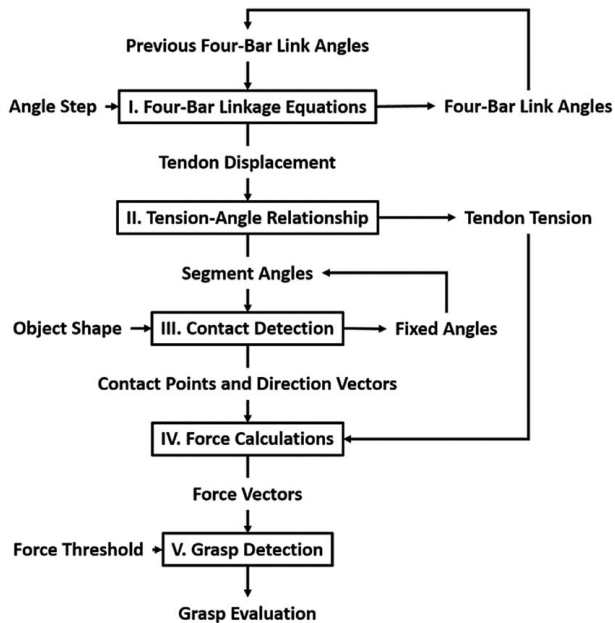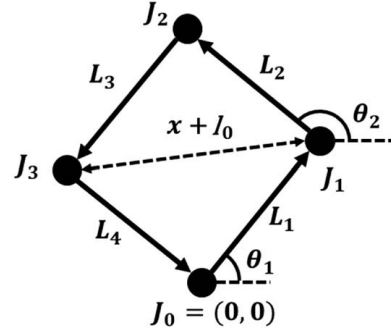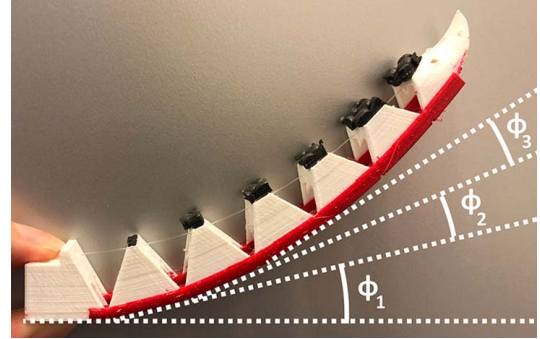

Fig. 10 Segment angles, ϕ_i, are the relative angles between consecutive segments of the foot

Fig. 8 Flowchart for the hybrid empirical–numerical model

Fig. 11 Setup for cable-tendon tension measurements. The tension is one half the force gage value because the tendon is looped once around the hook.

by displacing the cable tendon and photographing the resulting configuration. Angle values were extracted from the images using Logger Pro (Vernier Software Technology, Beaverton, OR); see Fig 12.

The best-fit cubic polynomials (based on data points that are averages of three measurements), shown in Figs. 13 and 14, for tendon tension, T (N), and relative segment angles, ϕ_i (degrees), as a function of tendon displacement, x (mm), were found to be

$$T(x) = 2.2790 \times 10^{-4} x^3 - 1.7690 \times 10^{-2} x^2$$
$$+ 5.7040 \times 10^{-1} x - 3.7080$$

$$\phi_1(x) = -3.3509 \times 10^{-4} x^3 - 1.0472 \times 10^{-2} x^2$$
$$+ 2.0563x + 4.5241$$

$$\phi_2(x) = -6.1532 \times 10^{-4} x^3 + 4.6033 \times 10^{-2} x^2$$
$$+ 1.7948 \times 10^{-1} x + 7.5518$$

$$\phi_3(x) = 2.6197 \times 10^{-4} x^3 + 2.8491 \times 10^{-3} x^2$$
$$+ 2.5346 \times 10^{-1} x + 4.2504 \qquad (6)$$

$$\phi_4(x) = 5.2187 \times 10^{-4} x^3 - 2.5865 \times 10^{-2} x^2$$
$$+ 8.9327 \times 10^{-1} x + 3.6461$$

$$\phi_5(x) = -5.9217 \times 10^{-5} x^3 + 1.1761 \times 10^{-2} x^2$$
$$- 5.0808 \times 10^{-2} x + 3.1368$$

$$\phi_6(x) = 2.2683 \times 10^{-4} x^3 - 4.1523 \times 10^{-3} x^2$$
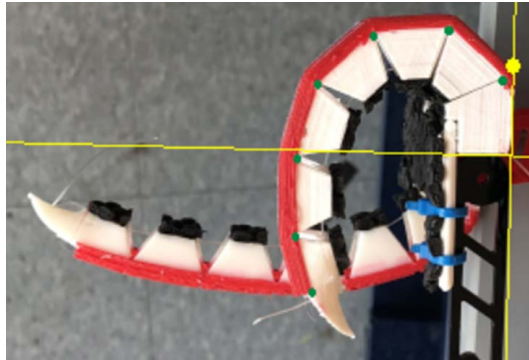$$+ 7.0504 \times 10^{-2} x + 3.4485$$

Fig. 12 Segment angles are determined using image analysis software. Segment vertices are annotated by hand.
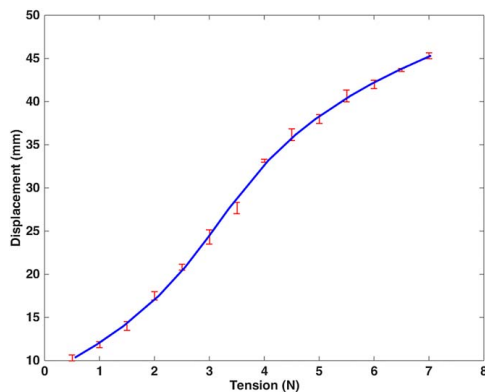

Fig. 13 Cubic polynomial curve fit for the measured tendon displacement as a function of tendon tension. Vertical bars identify the range of measured values.
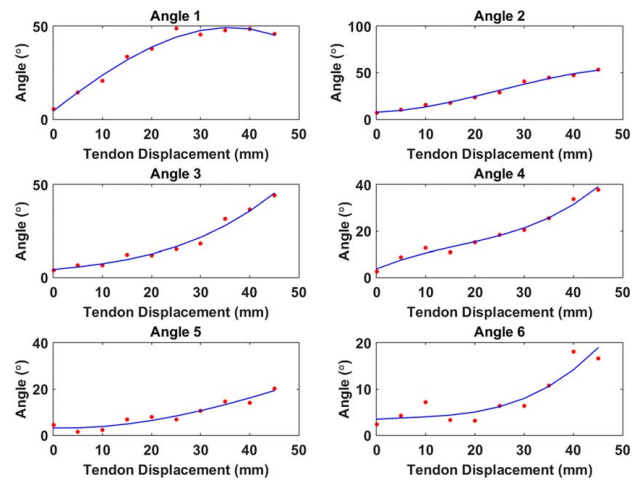

Fig. 14 Cubic polynomial curve fits for measured segment angles as a function of tendon displacement

3.3 Contact Detection. With the relative angles between segments known, the orientation of each segment can be constructed by transforming the points defining the segment's vertices by the appropriate angle and translating them such that each segment is positioned with respect to the previous segment as shown in Fig. 15. Angles greater than the maximum angle allowed by the foot geometry are capped at the maximum value. The same process is then repeated for the opposing foot but with the rotation angles reversed. The transformation is given in Eq. (7) where $P_{i,n}$ is the original vertex n of segment i, $P'_{i,n}$ is the transformed vertex, and $\phi_{i_{total}}$ is the sum of the first i segment angles. Figure 16
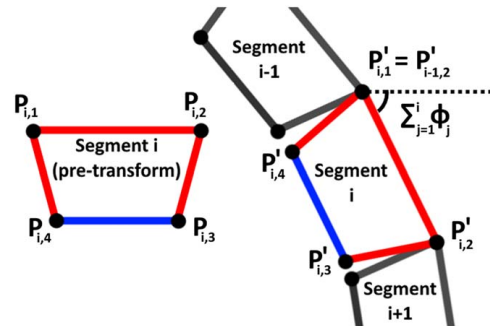

Fig. 15 A foot is assembled by rotating and translating each segment into its current position and orientation
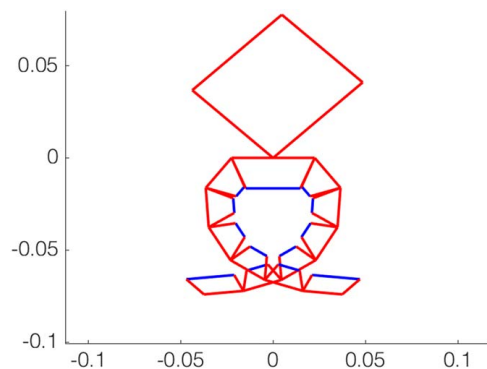

Fig. 16 Example configuration of the four-bar linkage and two feet. The undersides of the segments are used for contact detection.

shows an example configuration of the feet and the four-bar linkage.

$$P'_{i,n} = \begin{bmatrix} \cos(\phi_{i_{total}}) & \sin(\phi_{i_{total}}) \\ -\sin(\phi_{i_{total}}) & \cos(\phi_{i_{total}}) \end{bmatrix} P_{i,n} + (P'_{i-1,2} - P_{i,1}) \quad (7)$$

To detect contact between the foot segments and objects with polygonal cross sections, each edge of the polygon is tested for contact with the inner surface of each segment. The direction of the force vector exerted by the segment on the polygon is taken to be normal to the edge; except when the contact point (within a small tolerance) is a vertex of the polygon, then the direction of the force is normal to the inner surface of the segment; see Fig. 17 (left).

To detect contact between segments and circular cross sections, the center of the circle is orthogonally projected onto each foot segment. If the projected point lies both on the actuation and inside the circle, or if an endpoint of the segment is inside the circle, then the contact has occurred. As shown in Fig. 17 (right), the direction of the force points from the contact point toward the center of the circle.

3.4 Force Calculations. The net moment exerted by each segment on the object is zero immediately before that segment makes initial contact. At that instant, the moment of the previous segment acting on that segment is equal to the moment generated by the cable tendon. As tension increases after a segment has made contact, the moment created by the tendon on the segment increases. By subtracting the tendon moment when contact was first made from the tendon moment at a later state, the magnitude of the moment acting on the object can be determined from

$$M_T(x) = |r_T|T(x)\cos\left(\frac{1}{2}\phi_{max} - \frac{1}{2}\phi(x)\right) \text{ and} \quad (8)$$

$$M_F(x) = M_T(x) - M_E(x) = M_T(x) - M_T(x_c)$$
$$= |r_T|(T(x) - T(x_c))\cos\left(\frac{1}{2}\phi_{max} - \frac{1}{2}\phi(x)\right) \quad (9)$$

where $T(x)$ is the tendon tension, $M_T(x)$ is the moment applied by the tendon on the segment, $M_F(x)$ is the moment applied by the object on the segment, $M_E(x)$ is the moment applied on the segment by the previous segment (i.e., the moment from the elastic rails), x_c is the value of x when the segment first made contact with the object, and r_T is the displacement vector from the segment's pivot point to the point where the tendon enters the segment; see Fig. 18.

Starting with the claw end segment and moving to the base, if a subsequent segment has also made contact with the object, an
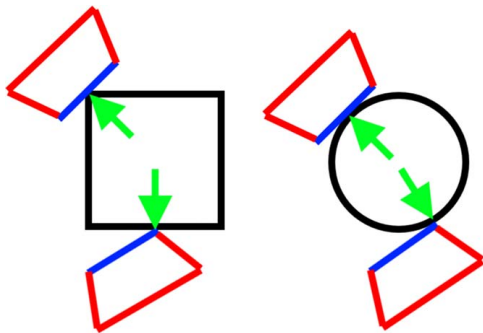

Fig. 17 Directions of contact forces applied by an object with a polygon (left) or circular (right) cross section to a foot segment
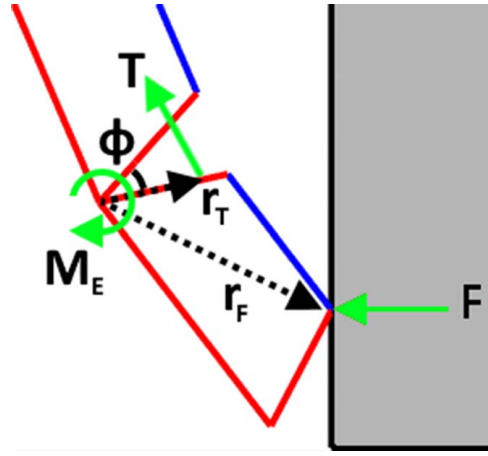
Fig. 18 The forces and moments acting on a foot segment that contributes to moment equilibrium with respect to the pivot point

additional moment exists and must be subtracted from M_F

$$M_{F_{net}} = M_F - \sum_{j=i+1}^{N} |r_{F_{ij}} \times F_j| \quad (10)$$

where $M_{F_{net}}$ is the moment created by the contact force, **F** (Fig. 18), between the object and segment i (only), $r_{F_{ij}}$ is the displacement vector between the pivot point of segment i and the contact point of the force of the object on segment j, and F_j is the force on segment j.

Given the moment exerted on the object and the direction vector of the applied force found during contact detection, the magnitude of the applied force can be computed from

$$F_i = \frac{M_{F_{net}}}{|r_{F_{ii}} \times \hat{F}_i|} \quad (11)$$

where $\hat{F}_i$ is a unit vector in the direction of the force and $r_{F_{ii}}$ is the position vector between the pivot point of the segment and the contact point of the segment with the object.

In addition, the active weight of the UAV (i.e., deadweight minus vertical lift force) acting on the linkage can be related to the geometric configuration of the feet through the tendon tension. The relationship of the tension, T, to the active weight, W, can be approximated by taking the lengths of all of the links to be equal as

$$W = T \tan(\beta) \sec(\alpha + \gamma) \text{ with}$$
$$\alpha = \frac{\theta_1 + \theta_4}{2} - 180° \text{ and } \beta = \frac{\theta_1 - \theta_4}{2} + 180° \quad (12)$$

where α is the angle between the horizontal centerline (connecting joints 1 and 3) of the linkage and the ground, β is the angle between the horizontal centerline and the first link, and γ is the approach angle, or the angle of the weight vector with respect to vertical; see Fig. 19. It is convenient to use the effective weight component, $W' = W \cos(\alpha + \gamma)$ and the compressive force in the links, $T/(2\cos(\beta))$, in deriving Eq. (12). The active weight of the UAV and the resulting tension are then related as

$$W_{max} = -T_{max} \tan\left(\frac{\theta_1 - \theta_4}{2}\right) \sec\left(\frac{\theta_1 + \theta_4}{2} + \gamma\right) \text{ or}$$
$$T_{max} = -W_{max} \cot\left(\frac{\theta_1 - \theta_4}{2}\right) \cos\left(\frac{\theta_1 + \theta_4}{2} + \gamma\right) \quad (13)$$
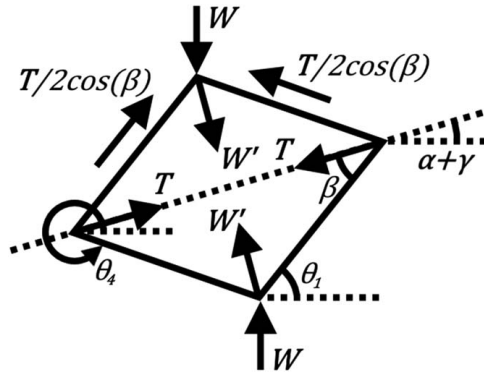
Fig. 19 Force diagram relating UAV weight and tendon tension. The weight *W* and the tendon tension *T* are forces applied to the linkage. The effective component of the weight is $W' = W\cos(\alpha + \gamma)$, and $T/(2\cos(\beta))$ is the compressive force in the linkage elements (shown acting on joint J_2).

The active weight of the UAV that produces the minimum force required to fully compress the four-bar linkage is referred to as the full-collapse weight. So that, if the active weight of the UAV is less than full-collapse weight, the linkage will not fully collapse when the UAV comes to rest. For the prototype system, the distance between joints 1 and 3 is 69 mm in the initial, unloaded configuration and 113 mm when the linkage is considered to be fully collapsed. Therefore, the maximum displacement of the tendon is 44 mm which corresponds to a tension of 6.6 N (see Fig. 13). From Eq. (13), that tension corresponds to a full-collapse weight of 2.6 N when the approach angle is zero.

3.5 Grasp Detection. Simulations begin with the tendon displacement equal to zero. As time evolves, the displacement is increased quasi-statically. When a foot segment comes into contact with the object, that segment along with all other segments between it and the heel, are fixed in place for the remainder of the simulation. When every segment becomes fixed in place, the legs (four-bar linkage) likewise become fixed because the tendon is unable to displace further. Note however that the tendon tension could still increase if the active weight of the UAV is greater than the collapse weight. The simulation ends when all of the feet segments become fixed in place or when the legs fully collapse, whichever occurs first.

3.5.1 Kinematic Evaluation of Enclosure. A kinematics-based metric has been created to evaluate whether the feet have enclosed the target object when the UAV is perched at the end of a simulation. A grasp configuration is defined as enclosed if the object is fully constrained, i.e., there are opposing contact forces (components) from the feet on the object in every direction. The grasp is defined as not enclosed if the object is not fully constrained, i.e., there is a direction in which the object could translate that is not opposed by a contact force (component); see Fig. 20.

Enclosure is determined as follows. The angles of the contact forces are calculated with respect to a Cartesian reference frame and are then sorted by signed magnitude as

$$\psi = \text{sort}\left(\left[\tan^{-1}\left(\frac{F_{y1}}{F_{x1}}\right), \tan^{-1}\left(\frac{F_{y2}}{F_{x2}}\right), \ldots, \tan^{-1}\left(\frac{F_{yN}}{F_{xN}}\right)\right]\right) \quad (14)$$

where F_{xi} and F_{yi} are the components of each contact force vector and ψ is the sorted list of force application angles. The differences between consecutive angles are computed as

$$\max\left([\psi_2 \ldots \psi_N, \; \psi_1 + 360^\circ] - [\psi_1, \; \psi_2 \ldots \psi_N]\right) < 180^\circ \quad (15)$$

If the grasp is enclosed, no consecutive angles have a difference greater than or equal to 180 deg.
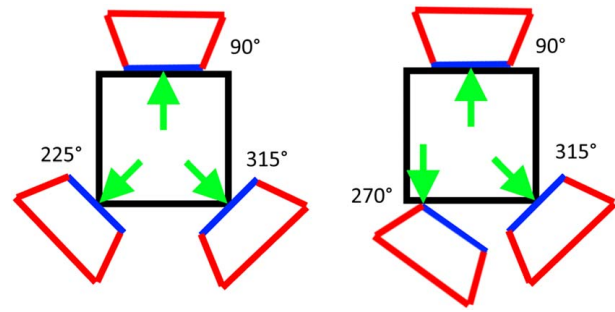

Fig. 20 Examples of an enclosed grasp (left) and a not-enclosed grasp (right) using the kinematic-based metric. The segments of the enclosed grasp have fully constrained the block. The not-enclosed grasp does not fully constrain the block motion to the left would be unopposed.

A (finite) characteristic value is used to denote an enclosed grasp. That value is referred to as the minimum UAV weight which is defined as the active weight of the UAV when the kinematic enclosure metric is first satisfied. If the grasp is not enclosed at the end of the simulation then the minimum weight of the UAV is reported to be undefined.

3.5.2 Kinetic Evaluation of Strength. A kinetics-based metric has been created to evaluate the success of a grasp and quantify its strength in terms of force. A grasp is defined as successful when the sums of the forces on the landing gear in each of the positive horizontal (+x), negative horizontal (−x), and downward (−y) directions are all greater than a specified threshold force value; see Fig. 21. If the sum of the forces in any of the three directions is below the threshold, the grasp is defined as not successful. This quantifies the strength of the grasp, i.e., the amount of force it would take to pull the landing gear off in one of the three directions. This metric is presented in terms of both the minimum UAV weight required to achieve a successful grasp and the minimum grip force, which is defined as the smallest of the three force summations at the end of the simulation. In order to calculate the sums, the contact forces on the landing gear are decomposed into horizontal and vertical components. In this case, the effective weight of the UAV is included as an additional force in the downward direction. If the
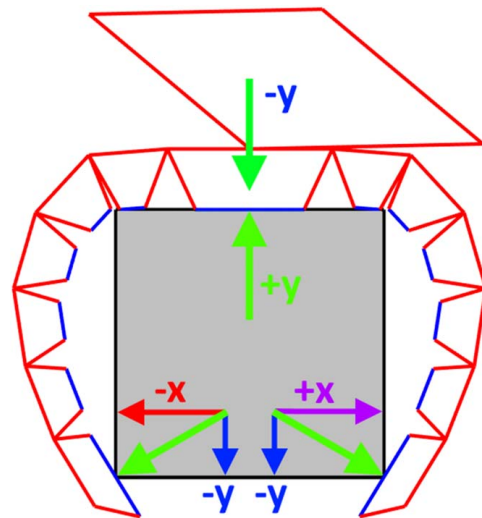

Fig. 21 Force diagram for the kinetics-based grasp metric. Contact forces on the landing gear are decomposed into horizontal and vertical components. The grasp is successful if the sums of the force components (including downward weight) in each cardinal direction are greater than a specified threshold value.

weight vector is angled (i.e., $\gamma \neq 0$), then the horizontal component of the weight is added or subtracted from the horizontal force sums as appropriate. The sum of the forces in the $+y$ (upward) direction is not evaluated because the UAV is taken to be on top of the target object and the UAV cannot be pushed through the object regardless the amount of force applied. The choice of the force threshold value depends on the expected operating loads acting on the UAV (e.g., wind, base motion). For example, a designer could determine the minimum weight of a UAV needed to maintain a perch on a branch of given size and shape when subject to a given wind force in any direction.

It is noted here that when the effective weight of the UAV is not included and the force threshold value is taken to be zero, the enclosure and success metrics yield the same results. In this limiting case, an enclosed grasp is successful while a not-enclosed grasp is not successful. In addition, this model simulates and evaluates grasping in terms of normal forces arising from contact between the feet and the target object. It does not account for any moment generated by the UAV on the object as it perches. In that case, it would be necessary to include forces tangent to the surface of the object, e.g., friction.

4 Grasping Simulations and Analysis

The model was used to create simulations of the landing gear engaging with various perches. Animations included in the "Supplemental Materials" for this paper on the ASME Digital Collection show the kinematic behavior of the feet as they enclose a series of objects with differently shaped cross sections. The right column of Fig. 22 shows the final configuration of the feet around a rectangle, off-center (relative to the UAV) rectangle, square, triangle, circle, and an empty grasp, respectively. The left column of Fig. 22 shows the final configuration of the prototype grasping the corresponding physical objects. In these cases, the approach angle is taken to be zero (i.e., weight vector is vertical). This side-by-side comparison clearly demonstrates the accuracy and validity of the model.

The model was then used to sweep through objects of the same shape with varying size, position, or rotation. Grasp cases were quantitatively characterized using both the enclosure and the strength metrics. In all of these cases, the deadweight of the UAV is taken to be the collapse weight (2.6 N) and the approach angle is taken to be zero. For the minimum UAV weight evaluation a force threshold value of 1.0 N was chosen as an example.

Figure 23 summarizes analyses of the grasp simulations. Plots in the left column characterize the enclosure of the grasp. The solid regions indicate cross section dimensions for which the target object is enclosed and are represented by the minimum UAV weight. The empty regions indicate dimensions for which the feet cannot enclose the object. Animations in the "Supplemental Materials" show enclosure results with green and red fill corresponding to an enclosed or not-enclosed grasp, respectively.

Plots in the two rightmost columns characterize the success of the grasp in terms of the minimum UAV weight and the minimum grip force, respectively. The cross sections (second column from left) corresponding to the plots in each row are (a) circle, (b) square, (c) triangle, (d) square rotated 30 deg with respect to horizontal, (e) square shifting horizontally to the left, and (f) rotating square. The solid regions in the success-weight column indicate dimensions for which the grasp is defined as successful while the empty regions correspond to regions where the grasp is not successful. The solid regions in the success-weight column coincide with the regions in the success-force column that have a value above the 1 N force threshold (dotted line).

4.1 Circular Cross Sections of Increasing Radius.
Results corresponding to circular cross sections of varying radii are shown in row a of Fig. 23. Sharp variations of weight or force occur when the number of segments in contact with the object
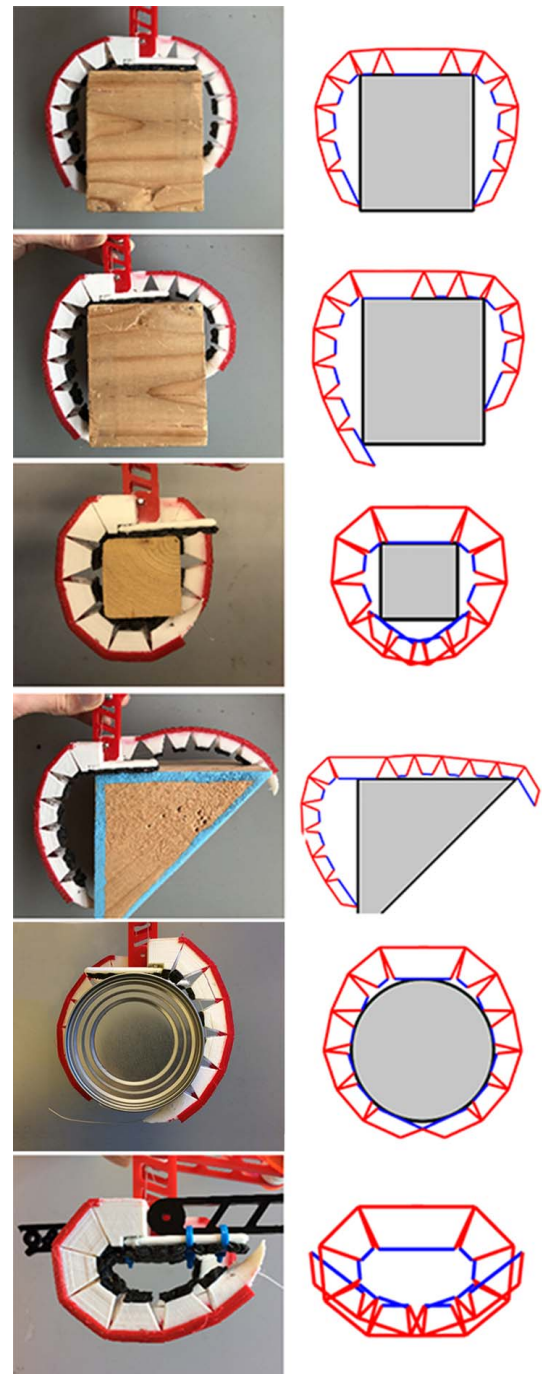

Fig. 22 Comparison of the simulated (right) and prototype's (left) grasp of a rectangular block, off-center rectangular block, small square block, triangular block, cylinder, and of an empty grasp

change. Kinematically, the circular cross section is fully enclosed when the radius is between 1.2 and 7.5 cm. Below 1.2 cm, the feet do not make sufficient contact with the circle. Above 7.5 cm, the feet cannot reach around far enough to make contact with the underside of the circle so as to provide a downward contact force on the landing gear. However, the grasp is successful even above 7.5 cm because, with the inclusion of gravity, the contact forces in the evaluated directions are greater than the threshold value. This is also the case with subsequent objects. For radii greater than 9.2 cm, the minimum weight is 2.6 N which is the same weight required to fully compress the linkage.
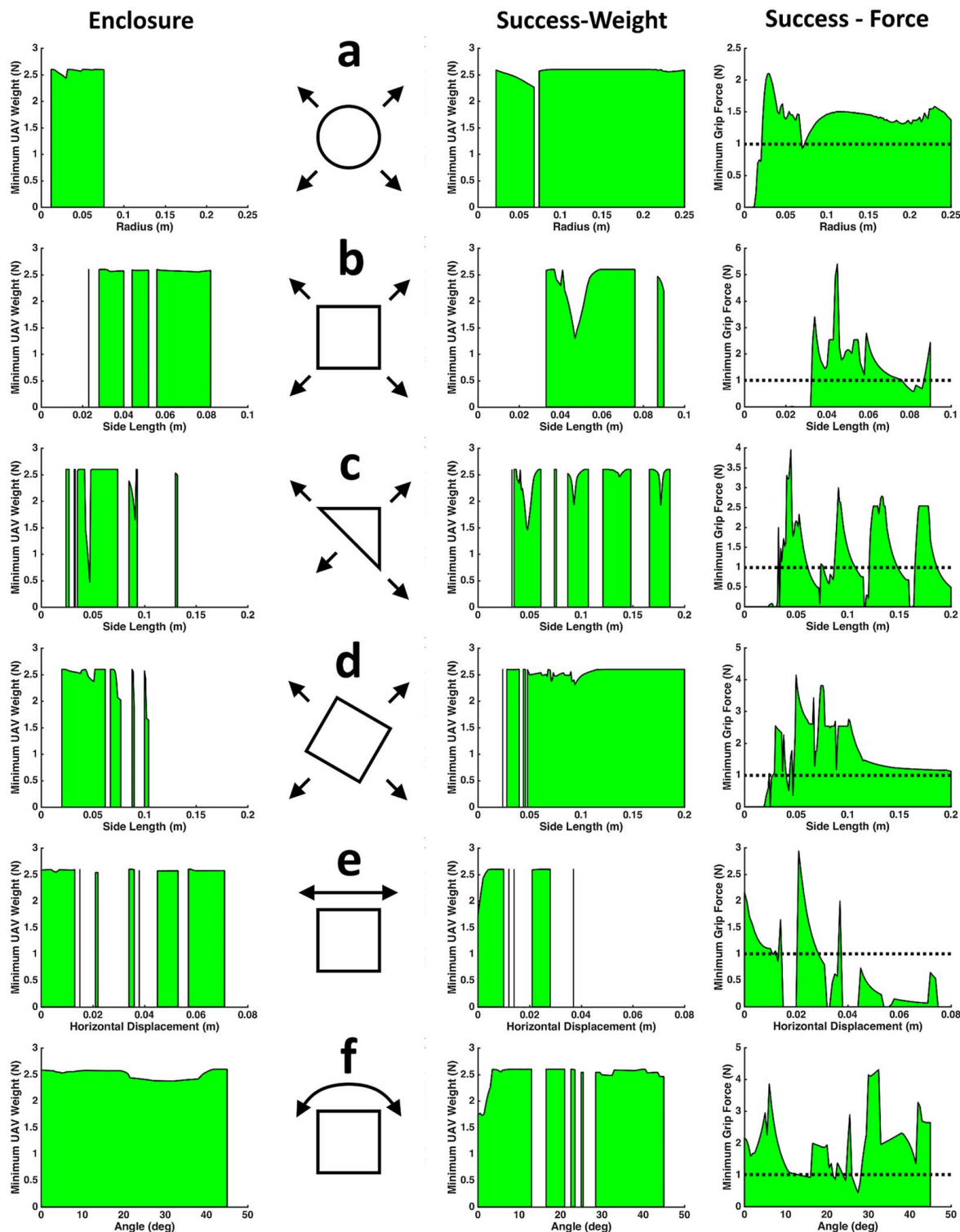
Fig. 23 Grasp analysis for various cross sections of increasing dimension or changing orientation (horizontal axes). Rows correspond to cross-sectional shapes: circle, square, triangle, square rotated 30 deg, square moving left relative to UAV, and rotating square, respectively. In the left column, solid areas indicate regions where the grasp encloses the objects and specify the minimum UAV weight. Grasp success (solid areas) is shown in the two right columns with the corresponding minimum UAV weight and grip force (above the threshold value 1.0 N), respectively.

4.2 Square Cross Sections With Increasing Side Length. Figure 23 row b shows results for square cross sections with varying side length. The grasp is enclosed for side lengths between 2.8 and 8.0 cm, except in regions where the corners of the square slip into the gaps between segments of the feet. Grasps are still successful in these cases, however, because the force of gravity is sufficient to constrain the landing gear vertically. The grip force varies considerably as different foot segments become engaged.

4.3 Triangle Cross Sections With Increasing Side Lengths. Results for an isosceles right triangular cross section of varying

side lengths are shown in row c of Fig. 23. For side lengths primarily between 3.5 and 7.4 cm, the grasp is enclosed because one foot can curl around underneath the lower vertex of the triangle. Above 7.4 cm, there are multiple additional regions of grasp enclosure. There is a wider range where the grasp is denoted as successful. This occurs, again, because of the inclusion of weight and because foot segments become hooked around the triangle's two upper vertices, applying a constraining force in the horizontal or, in some cases, the vertical direction (see animation).

4.4 Square Cross Sections Rotated Relative to Horizontal With Increasing Side Length. In Fig. 23 row d, results are shown for a square cross section of varying side length. In this case, the square is oriented such that one side is at a 30-deg angle with respect to horizontal. In comparison with the non-rotated square, the grasp is enclosed over a larger range as the angled sides provide a reachable contact surface on which the feet can apply an upward constraining force. The grasp is also successful over larger side lengths because the angled surfaces provide a horizontal contact force component even when the feet can no longer reach around the square's vertices.

4.5 Square Cross Sections of Fixed Size With Shifting to the Left. In Fig. 23 row e, results are shown corresponding to a square cross section of fixed size (side length = 5 cm) shifting horizontally to the left with respect to the landing gear. The landing gear is able to consistently enclose the square cross section for horizontal offsets up to 1.3 cm. As the square shifts, grasp success is consistent up to 1 cm. The minimum grip force depends upon whether the corners of the square slip into the spaces in between segments of the feet.

4.6 Square Cross Sections of Fixed Size Rotating About its Center. Figure 23 row f shows results for a square with a side length of 5 cm as the square rotates about its centroid. The grasp is enclosed at every (unique) angle with a sharp peak in grip force at 6 deg but regions of lower grip force between 13 and 16 deg, at 22 and 24 deg, and between 26 and 28 deg where the grasp is unsuccessful.

4.7 Increasing Approach Angle. An example of the effect that variations in approach angle, γ, have on grasp success (as defined in Sec. 3.5.2) with respect to a cylindrical cross section (radius = 5 cm) is presented in Fig. 24. The left plot shows that the grasp is successful when the UAV is vertical (approach angle = 0) with a corresponding minimum UAV weight of 2.43 N. As the approach angle increases, the grasp remains successful only if the minimum UAV weight can likewise increase (because the component of weight in the vertical direction decreases). At angles greater than 8 deg, however, the grasp criteria cannot be met regardless of UAV weight because the horizontal component of the

gravity force increases faster than the horizontal contact forces as more weight is applied. The plot on the right corresponds to the prototype system with the UAV weight of 2.6 N. As the approach angle increases from vertical, the force needed to dislodge the feet decreases quickly and drops to zero at 22 deg.

5 Experimental Demonstrations

Experiments were conducted with prototypes of the landing gear system to evaluate their perching capability and performance. A hexacopter (Flame Wheel F550, DJI, Shenzhen, China) was chosen as the test platform because of its ready availability, customizability, and reasonable cost. The mass of the frame is 478 g and has a diagonal wheelbase of 550 mm. The takeoff mass is between 1200 and 2400 g with a payload of 700 g and 900 g when the recommended motors, batteries, and electronics are used.

5.1 Resting Perch. The first series of experiments demonstrated that the landing gear enabled the hexacopter airframe, with battery packs attached to represent the mass of an operable aircraft, to stably perch on different objects. After the frame was lowered onto the target object and the leg locks engaged, it was left to perch upright on its own. Figure 25 shows resting perches on a horizontal PVC pipe (top), on a rectangular metal railing (middle), and standing on the edge of a stone wall ledge (bottom). Figure 26 shows the suspended, loaded airframe being manually lowered onto a 2 × 4 wood beam (top) and an asymmetric branch of a tree (bottom). When the frame was lifted up, the locked grasp was sufficiently strong to carry the wood beam.

5.2 Disturbance Rejection. A second set of experiments demonstrated that the landing gear was able to maintain its grasp under disturbance to the perch. The landing gear mechanism was engaged and locked on the arm of a chair; see Fig. 27. The chair was then shaken vigorously by hand; see video in the "Supplemental Materials."

5.3 Flight Tests. In a third set of experiments, the hexacopter frame was fully outfitted (Fig. 28) and flown under radio control. Similar to the manually lowered landings, the hexacopter was to be piloted over the perch and set down such that its weight would collapse the linkage as it came to rest; however, we were not able to fly the hexacopter into a properly aligned position or slow down enough to come to rest on the target object. In contrast, takeoff tests from a resting perch were successful. The pilot could disengage the leg lock and lift off as the hexacopter released its grasp; see sequence shown in Fig. 29. There were no problems flying the drone with the landing gear system attached.
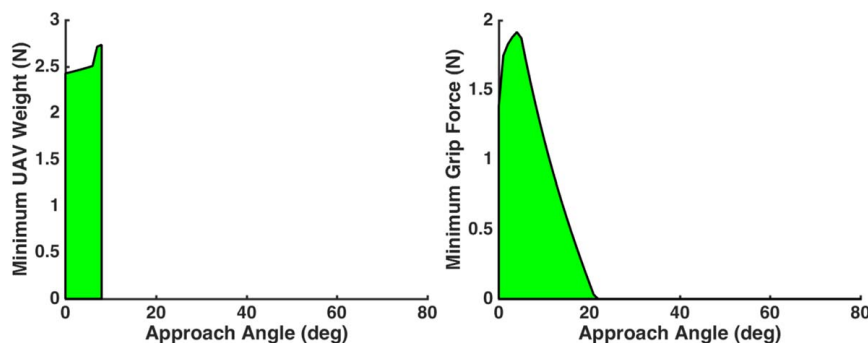

Fig. 24 Analysis of grasp success in terms of the angle with which the UAV approaches the perch (i.e., approach angle). Solid areas indicate success. The shape of the perch is circular (radius = 5 cm). The threshold force is set at 1.0 N.

Fig. 25 Demonstration of perching on a PVC pipe (top), a metal hand railing (middle), and the side of a stone ledge (bottom). The legs are attached directly to the hexacopter frame. Weights were added to simulate a fully loaded rotorcraft.

5.4 Scalability. The scalability of the perching landing gear system is being investigated. A scaled-down, conceptual design has been created for a small quadcopter, the Dromida Ominus (Hobbico Inc., Champaign, IL); see CAD render in Fig. 30 (top row). The Ominus has a mass of 100 g and a diagonal span of 238 mm. Based on flight tests, it can take off and be flown with a payload up to approximately 60 g. In order to make the landing gear compact, the two legs are combined into a single multi-link leg with two separated sets of opposing feet. As with the larger-scale

design, the feet are single, compliant structures. However, in this case solid, ABS segments are integrated into a tapered NinjaFlex beam; see Fig. 30 (bottom row). The length of the links is approximately 2.5 cm and the overall mass of the linkage is 20.3 g. The mass of one foot is 1.1 g. Figure 31 shows a grasping sequence of a fabricated pair of feet as a threaded cable tendon is pulled manually. An empirical–numerical model of this prototype can be created using the methodology described herein to evaluate its grasping capability and to identify the range of objects it can perch on.

Fig. 26 Landing sequence of the suspended, weighted hexacopter frame as it is lowered onto a wood board (top) and a tree branch (bottom). The feet grasp the object and the legs are locked in place.
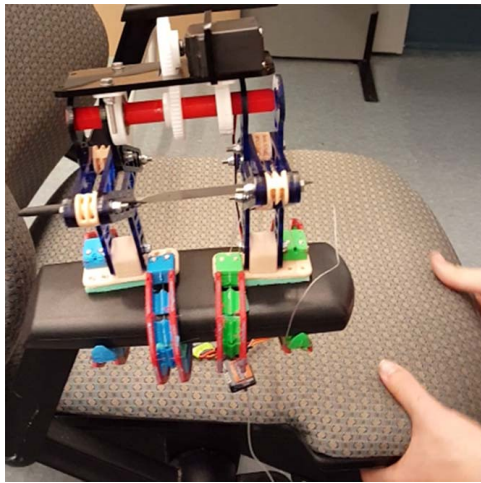
Fig. 27 Landing gear perched on the arm of a chair. With the lock engaged, the mechanism maintains its grasp when the chair is vigorously shaken.

Fig. 30 Design concept for a smaller-scale perching landing gear. CAD **renders (top). Photos (bottom) of the four-bar linkage mechanism and the end of one foot.**

Fig. 28 Fully outfitted hexacopter perching on a tree branch. Struts were added to the frame to protect the body.

6 Conclusion

This paper describes the design, modeling, simulation, and testing of a landing gear system for a small UAV which enables it to perch upon branches or similar structures. The landing gear has an opposing, multi-segment feet to grasp the perch target. In a way similar to some birds, the feet are actuated by cable tendons that are pulled in tension by a four-bar linkage that collapses as the UAV lands. In order to determine objects of different shapes and sizes on which a fabricated prototype could perch, a hybrid empirical–numerical model which can be used to simulate
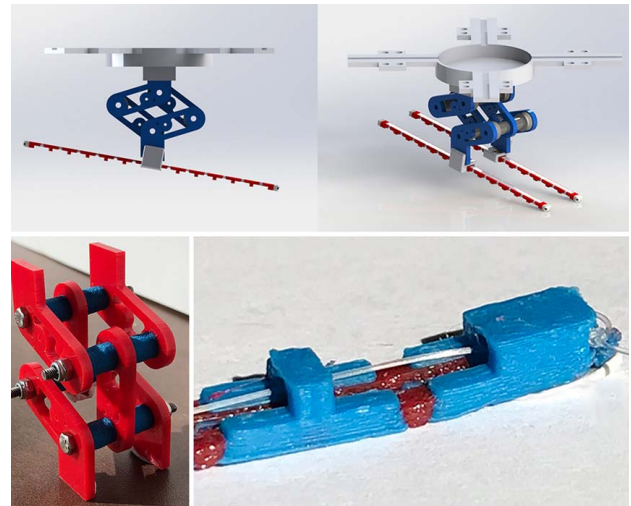
grasping behavior was created. Analysis of the simulation results explains how and why the grasp encloses a given cross section and is successful based on kinematic and kinetic metrics. This model is a general tool which can be used by UAV designers to identify objects and structures on which the air vehicle can land, perch, and takeoff. Using this information, missions can be tailored for specific environments. In addition, the hybrid empirical–numerical approach bypasses the need for computational-intensive physics-based techniques, e.g., finite element analysis using nonlinear material models.

Prototype landing gear systems were fabricated and integrated with a radio-controlled hexacopter. Experiments validate the results of the simulations and showed that the hexacopter could land, perch (even when subject to significant disturbance), and take off from a range of objects. These results demonstrate the feasibility of this perching landing gear design. Giving a UAV the capability to perch greatly expands its utility and functionality. The next steps in continuing this work are to carry out the grasp simulation, analysis, and experimental verification for the smaller-scale perching landing gear system and to continue development and integration to create operational UAVs.

Fig. 29 Hexacopter takeoff sequence starting from a resting perch (left)
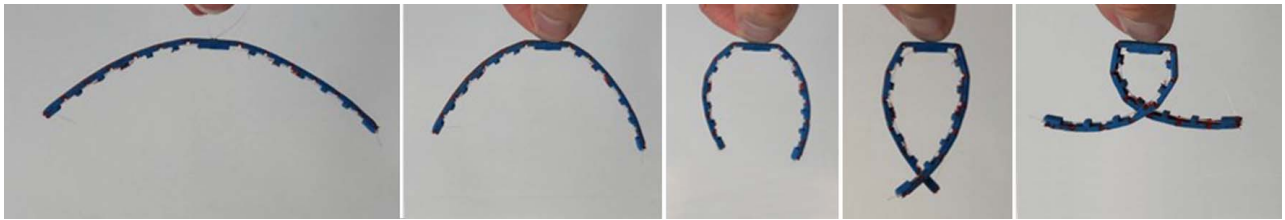
Fig. 31   Grasping sequence of a pair of feet as the tendon is pulled manually

Nomenclature

x = tendon displacement

F = contact force vector of the grasped object on a foot segment

J = coordinates for a vertex of the four-bar linkage

L = length of a link in the four-bar linkage

P = coordinates for a vertex of a foot segment

T = tendon tension

W = effective weight of the UAV applied to the four-bar linkage

r_F = displacement vector from a foot segment's pivot point to the point of application of a contact force of the grasped object on the foot segment

r_T = displacement vector from a foot segment's pivot point to the point where the tendon enters the segment

x_c = tendon displacement when a foot segment first comes into contact with the grasped object

L_0 = distance between joints J_1 and J_3 in the four-bar linkage's initial configuration

M_E = moment applied by a previous segment to a foot segment

M_F = moment applied by the grasped object to a foot segment

M_T = moment applied by the tendon to a foot segment

α = angle between the horizontal centerline of the four-bar linkage and the ground

β = angle between the horizontal centerline of the four-bar linkage and the first link

γ = approach angle of the UAV with respect to vertical

θ = angle of a link in the four-bar linkage relative to the horizontal

ϕ = relative angle between two consecutive foot segments

ψ = angle of application of a contact force of the grasped object on the foot segment

ω = angular velocity of a link in the four-bar linkage

References

[1] Nadan, P. M., and Lee, C. L., 2018, "Computational Design of a Bird-Inspired Perching Landing Gear Mechanism," ASME International Mechanical Engineering Congress & Exposition (IMECE), Pittsburgh, PA, Nov. 9–15, ASME Paper No. IMECE2018-86615.

[2] Tieu, M., Michael, D. M., Pflueger, J. B., Sethi, M. S., Shimazu, K. N., Anthony, T. M., and Lee, C. L., 2016, "Demonstrations of Bio-Inspired Perching Landing Gear for UAV's," Proceedings of the SPIE 9797 Bioinspiration, Biomimetics, and Bioreplication, Las Vegas, NV, Mar. 20–24, Paper No. 9797X.

[3] Kovac, M., 2016, "Learning From Nature How to Land Aerial Robots," Science, **352**(6288), pp. 895–896.

[4] Robertson, D. K., and Reich, G. W., 2013, "Design and Perching Experiments of Bird-Like Remote Controlled Planes," 54th AIAA/ASCE/AHS/ASC Structures, Structural Dynamics, and Materials Conference, Boston, MA, Apr. 8–11, AIAA Paper No. AIAA 2013-1788.

[5] Nagendran, A., Crowther, W., and Richardson, R. C., 2012, "Biologically Inspired Legs for UAV Perched Landing," IEEE Aerosp. Electron. Syst. Mag., **27**(2), pp. 4–13.

[6] Paranjape, A. A., Kim, J., Gandhi, N., and Chung, S.-J., 2011, "Experimental Demonstration of Perching by an Articulated Wing MAV," AIAA Guidance, Navigation, and Control Conference, Portland, OR, Aug. 8–11, AIAA Paper No. AIAA 2011-6403.

[7] Cory, R., and Tendrake, R., 2008, "Experiments in Fixed-Wing UAV Perching," AIAA Guidance, Navigation, and Control Conference, Honolulu, HI, Aug. 18–21, AIAA Paper No. AIAA 2008-7256.

[8] Culler, E. S., Thomas, G. C., and Lee, C. L., 2012, "A Perching Landing Gear for a Quadcopter," 53rd AIAA/ASCE/AHS/ASC Structures, Structural Dynamics, and Materials Conference, Honolulu, HI, Apr. 23–26, AIAA Paper No. AIAA 2012-1722.

[9] Ali Erbil, M., Prior, S. D., and Keane, A. J., 2013, "Design Optimisation of a Reconfigurable Perching Element for Vertical Take-Off and Landing Unmanned Aerial Vehicles," Int. J. Micro Air Veh., **5**(3), pp. 207–228.

[10] Chi, W., Low, K. H., Hoon, K. H., and Tang, J., 2014, "An Optimized Perching Mechanism for Autonomous Perching With a Quadrotor," IEEE International Conference on Robotics and Automation (ICRA), Hong Kong, China, May 31–June 7, pp. 3109–3115.

[11] Jiang, H., Pope, M. T., Hawkes, E. W., Christensen, D. L., Estrada, M. A., Parlier, A., Tran, R., and Cutkosky, M. R., 2014, "Modeling the Dynamics of Perching With Opposed-Grip Mechanisms," International Conference on Robotics and Automation (ICRA), Hong Kong, China, May 31–June 7, pp. 3102–3108.

[12] Burroughs, M. L., Beauwen Freckleton, K., Abbott, J. J., and Minor, M. A., 2015, "A Sarrus-Based Passive Mechanism for Rotorcraft Perching," ASME J. Mech. Rob., **8**(1), p. 011010.

[13] Quinn, T. H., and Baumel, J. J., 1990, "The Digital Tendon Locking Mechanism of the Avian Foot (Aves)," Zoomorphology, **109**(5), pp. 281–293.

[14] Backus, S. B., Odhner, L. U., and Dollar, A. M., 2014, "Design of Hands for Aerial Manipulation Actuator Number and Routing for Grasping and Perching," IEEE/RSJ International Conference on Intelligent Robots and Systems, Chicago, IL, Sept. 14–18, pp. 34–40.

[15] Backus, S. B., Sustaita, D., Odhner, L. U., and Dollar, A. M., 2015, "Mechanical Analysis of Avian Feet: Multiarticular Muscles in Grasping and Perching," Royal Soc. Open Sci., **2**(2), Article ID 140350.

[16] Doyle, C. E., Bird, J. J., Isom, T. A., Kallman, J. C., Bareiss, D. F., Dunlap, D. J., King, R. J., Abbott, J. J., and Minor, M. A., 2013, "An Avian-Inspired Passive Mechanism for Quadrotor Perching," IEEE/ASME Trans. Mechatron., **18**(2), pp. 506–517.

[17] Xie, P., and Ma, O., 2013, "Grasping Analysis of a Bio-Inspired UAV/MAV Perching Mechanism," ASME International Mechanical Engineering Congress and Exposition (IMECE), San Diego, CA, Nov. 15–21, ASME Paper No. IMECE2013-66526.

[18] Xie, P., Ma, O., Zhang, L., and Zhao, Z., 2015, "A Bio-Inspired UAV Leg-Foot Mechanism for Landing, Grasping, and Perching Tasks," AIAA Atmospheric Flight Mechanics Conference, Kissimmee, FL, Jan. 5–9, AIAA Paper No. AIAA 2015-1689.

[19] Gardner, J. F., 2001, Simulations of Machines Using MATLAB and SIMULINK, Brooks/Cole, Pacific Grove, CA, Chap. 2–3.